arXiv:1603.04069v1 [cond-mat.mes-hall] 13 Mar 2016

Ballistic Majorana nanowire devices

Hao Zhang,[1,2,*] Önder Gül,[1,2,*] Sonia Conesa-Boj,[1,2,3] Kun Zuo,[1,2] Vincent Mourik,[1,2]
Folkert K. de Vries,[1,2] Jasper van Veen,[1,2] David J. van Woerkom,[1,2] Michał P. Nowak,[1,2]
Michael Wimmer,[1,2] Diana Car,[3] Sébastien Plissard,[2,3] Erik P. A. M. Bakkers,[1,2,3] Marina Quintero-Pérez,[1,4]
Srijit Goswami,[1,2] Kenji Watanabe,[5] Takashi Taniguchi,[5] and Leo P. Kouwenhoven[1,2,†]

[1]*QuTech, Delft University of Technology, 2600 GA Delft, The Netherlands*
[2]*Kavli Institute of Nanoscience, Delft University of Technology, 2600 GA Delft, The Netherlands*
[3]*Department of Applied Physics, Eindhoven University of Technology, 5600 MB Eindhoven, The Netherlands*
[4]*Netherlands Organisation for Applied Scientific Research (TNO), 2600 AD Delft, The Netherlands*
[5]*Advanced Materials Laboratory, National Institute for Materials Science, 1-1 Namiki, Tsukuba, 305-0044, Japan*

Majorana zero modes are quasiparticles emerging at the boundary of a topological superconductor[1–3]. Following proposals for their detection in a semiconductor nanowire coupled to a superconductor[4,5], several electron transport experiments reported characteristic Majorana signatures[6–10]. The prime challenge to strengthen these signatures and unravel the predicted topological properties of Majoranas is to reduce the remaining disorder in this hybrid system. First of all, disorder at or near a superconductor-semiconductor interface can mimic some of the zero-energy signatures of Majoranas[11–15]. Moreover, disorder can result in states at finite energy but still inside the induced superconducting energy gap[16]. This so-called soft-gap renders the topological properties experimentally inaccessible[17,18]. Here, we report significant improvements in reducing both types of disorder. From structural and chemical analyses, we show a high-quality interface between an InSb nanowire and a NbTiN superconductor. The low-temperature properties demonstrate ballistic transport based on observing a quantized conductance for normal carriers and a strong enhancement of conductance resulting from Andreev reflection. Gate tuning the device to a tunnel probe reveals an induced *hard*-gap with a strongly reduced subgap density of states. Spatial control of carrier density using local gates and an application of a magnetic field induces a zero bias peak that is rigid over a large region in the parameter space of gate voltage and magnetic field. These observations are consistent with the Majorana theory, and exclude alternative explanations based on disorder related effects.

Good electrical contact between a superconductor and semiconductor opens a gap in the semiconductor density of states generally referred to as the induced superconducting gap, Δ^*. The size of Δ^* depends sensitively on the transparency between the two materials. Spatial variations in this transparency result in spatial variations of the gap leading to a residual subgap density of states when averaged over a larger region[16]. In a topological superconductor these subgap states can interact with the zero-energy states, effectively destroying the topological properties of these Majorana modes[17,18]. Interface properties were dramatically improved in a recent demonstration of epitaxial growth of an Al superconductor on an InAs nanowire, resulting in a strongly reduced subgap density of states[19]. Further studies on this materials combination indeed showed improved Majorana signatures[20]. The InAs nanowire itself still contains residual disorder showing up in transport as unintentional quantum dots[14,15,19]. As an alternative materials system we have further developed the combination of InSb nanowires with NbTiN as our preferred choice of superconductor. InSb is in general cleaner (i.e. higher electron mobility[21–23]) than InAs. Moreover, InSb has a ~ 5 times larger g-factor, bringing down the required external magnetic field needed to induce the topological phase transition. Our preference for NbTiN relies on its high critical magnetic field (type-II), exceeding the 10 Tesla scale.

Here we present a nanofabrication recipe yielding largely improved InSb-NbTiN interfaces. We report on seven devices with different geometries all showing consistent results. An overview of all the devices is given in Supplementary Figures 3 and 4. Figure 1a shows a basic nanowire device consisting of a normal contact (Au), a nanowire (InSb) and a superconducting contact (NbTiN). This device was first measured at low temperature showing high-quality electron transport (data discussed below). After, the device was sliced open (using focused ion beam) and inspected sideways in a transmission electron microscope. The hexagonal facet structure of the nanowire is clearly visible (Figure 1c and Supplementary Figure 1). Except for the bottom facet that rests on the substrate, the polycrystalline superconductor covers the nanowire all around without creating any visible voids.

The precise procedure for contact deposition is extremely important. First the native oxide at the InSb surface is wet-etched using a Sulfur-based solution fol-

*These authors contributed equally to this work.
†Electronic address: L.P.Kouwenhoven@tudelft.nl

lowed by an Argon etch of sufficiently low-power to avoid damaging the InSb surface (see Methods). The inclusion of Sulfur at the interface results in band bending with electron accumulation near the surface of InSb (see Supplementary Figure 2). Superconducting film deposition starts with NbTi, a reactive metal whose inclusion as a wetting layer is crucial to create a good electrical contact. Figure 1d (details in Supplementary Figure 1) shows that our cleaning and deposition procedure leaves the InSb crystal structure intact. We detect a thin segregation layer ($\sim 2\,\mathrm{nm}$) between the polycrystalline NbTi and single crystalline InSb. The chemical analyses (Figure 1e and f) show materials content in agreement with our deposition procedure. More importantly, the inclusion of Sulfur is clearly visible at the interface whereas the original native oxide is completely absent.

The high-quality structural properties in Figure 1 result in largely improved electronic properties. Figure 2a shows the differential conductance $\mathrm{d}I/\mathrm{d}V$ while varying the bias voltage V between the normal and superconducting contacts, and stepping the gate voltage V_{gate} applied to the global back gate (Figure 1b). We first of all note that throughout the entire gate voltage range in Figure 2 we do not observe signs of the formation of unintentional quantum dots or any other localization effects resulting from potential fluctuations. Instead, we observe conductance plateaus at $2e^2/h$ for all devices, i.e. typical for ballistic transport and a clear signature of a disorder-free device. For a sufficiently negative gate voltage the non-covered nanowire section between normal and superconducting contacts is depleted and serves as a tunnel barrier. A vertical line cut from this regime is plotted in the lower panel of Figure 2b, showing a trace typical for an induced superconducting gap with a strong conductance suppression for small V. The extracted gap value is $\Delta^* = 0.8\,\mathrm{meV}$. Increasing V_{gate} first lowers and then removes the tunnel barrier completely. A vertical line cut from this open regime is plotted in the upper panel in Figure 2b. In this case, the conductance for small V is enhanced compared to the value above $\sim 1\,\mathrm{mV}$. Note that the range in V showing an enhanced conductance in the upper panel corresponds to the same range showing the induced gap in the lower panel. The enhancement results from Andreev processes where an incoming electron reflects as a hole at the NS interface generating a Cooper pair[24]. This Andreev process effectively doubles the charge being transported from e to $2e$ *enhancing* the subgap conductance. In Figure 2b the observed enhancement is by a factor ~ 1.5.

The Andreev enhancement is also visible in horizontal line cuts as shown in Figure 2c. The above-gap conductance (black trace) taken for $|V| = 2\,\mathrm{mV}$ represents the conductance for normal carriers, G_{n}. The subgap conductance, G_{s}, near $V = 0$ (Figure 2c, red trace) again shows an Andreev enhancement in the plateau region. The panels in Figure 2d and e show exemplary traces from two other devices. The enhancement in Figure 2d reaches $1.9 \times 2e^2/h$, very close to the theoretical limit: an enhancement factor of 2 in the case of a perfect interface. The plateau in G_{n} in Figure 2e is particularly flat whereas G_{s} shows a pronounced dip on the right-side of the plateau. The dip structure provides a handle for estimating the remaining disorder by a comparison to theory, as discussed below.

The theory for electronic transport from a normal conductor via a quantum point contact to a superconductor was developed by Beenakker[24]. The subgap conductance is described by Andreev reflections, and for a single subband given by $G_{\mathrm{s}} = 4e^2/h \times T^2/(2-T)^2$. The gate voltage dependent transmission probability T can be extracted from the measured above-gap conductance, given by $G_{\mathrm{n}} = 2e^2/h \times T$. Figure 3a shows excellent agreement between the calculated and measured subgap conductance up to the point where the measured Andreev enhancement is reduced causing the dip on the right side of the plateau. A numerical modelling (details in Supplementary Information) finds that the dip is caused by a mixing between the first and the second subband due to residual disorder. Even for weak disorder, mode mixing is strongly enhanced near the opening of the next channel, due to the van Hove singularity at the subband bottom. Hence, the Andreev conductance will generically exhibit a dip close to the next conductance step, instead of a perfect doubling. We find good agreement with our data (compare Figures 2e and f) for a mean free path of several μm. Given that our proximitized nanowire length is about $1\,\mu$m, this implies ballistic transport of Andreev pairs.

Besides deducing ballistic transport inside the nanowire, the Andreev enhancement allows for extracting the highest transmission, which sets a lower bound on the interface transparency. An enhancement factor of 1.4 implies $T > 0.9$ and our record value of 1.9 gives $T > 0.98$ (see Methods). The comparison between G_{s} versus G_{n} can be continued into the regime of an increasing tunnel barrier. Figures 3c and d show traces of $\mathrm{d}I/\mathrm{d}V$ for successively lower conductances. The subgap conductance suppression reaches $G_{\mathrm{s}}/G_{\mathrm{n}} \sim 1/50$, a value comparable to the results obtained with epitaxial Al[19]. A comparison between the measured subgap conductance and Beenakker's theory (without any fit parameters) is shown in Figure 3b. The excellent agreement over three orders of magnitude in conductance implies that the subgap conductance is very well described by Andreev processes and no other transport mechanisms are involved[19]. The lowest conductance ($\sim 5 \cdot 10^{-4} \times 2e^2/h$) reaches our measurement limit, causing the deviation from theory. The inset to Figure 3b shows how the subgap conductance increases when applying a magnetic field, which can be expected qualitatively since Beenakker's theory requires time reversal symmetry. A quantitative understanding of such magnetic field induced subgap transport, although very important, is outside the scope of this Letter.

The absence of unintentional quantum dots, the observed hard gap, quantized conductance and high

interface-transparency all result from our improved fabrication process. These advances have been included in devices with local gate electrodes that allow for a separate tuning of the chemical potential in the wire section underneath the superconducting contact independent from the tunnel barrier.

This spatial gate tunability allows us to explore the Majorana regime. Figure 4a shows an electron micrograph of a typical device where the three individual gates tune the electron density below the normal and superconducting contacts as well as the tunnel barrier. After tuning these gate voltages we find a regime (Figure 4b) where increasing the magnetic field closes the induced gap and induces a zero bias peak (ZBP) rigidly bound to $V = 0$ up to at least 1 Tesla. The gap closure observed at 0.38 T is expected to occur when $\Delta^* \sim E_z$ yielding $g \sim 40$, extracted from linear interpolation, which matches independent measurements[23]. Converting the magnetic field B axis into a Zeeman energy scale, we find that the ZBP is bound to zero over an energy range that is an order of magnitude larger than the peak width (the full width at half maximum, FWHM ~ 0.05 meV). This excludes a normal level-crossing as the origin for our ZBP. We note that the maximum ratio of ZBP-range/FWHM we have ever measured is close to two orders of magnitude[25].

The ZBP can be spatially resolved by varying the voltages applied on individual gates. Figure 4c shows that the ZBP exists only over a finite range in voltage applied to the super gate, meaning that proper tuning of the electron density underneath the superconducting contact is essential for the appearance of the ZBP. Figure 4d shows that changing the tunnel barrier conductance by more than a factor of three does not split the ZBP, nor makes it disappear. This implies that the ZBP does not result from physics occurring in or around the tunnel barrier (e.g. due to the '0.7 anomaly'[26] or from a weak antilocalization effect[12]). Figure 4e shows that a large variation in the voltage on the normal gate can modulate the overall conductance (e.g. affect interferences) but it does not remove the ZBP. The combined panels Figures 4c-e demonstrate that the ZBP originates on the superconducting side.

Different devices show differences in the detailed transport properties but the general behavior shown in Figure 4 is reproduced in all our devices with properly working contacts and local gate electrodes. Figure 5 illustrates the behavior of a device similar to the one in Figure 4a but with an induced gap significantly larger than the device in Figure 4. As a result, the induced gap closes at a higher magnetic field. In this example the ZPB is visible and un-split over a range in Zeeman energy larger than 1.5 meV. The FWHM is around 0.05 meV yielding a ratio ZBP-range/FWHM ~ 30. We again find that the ZBP is robust against a change in the barrier gate voltage which, in this case, changes the conductance over more than an order of magnitude (see Supplementary Figure 7).

In conclusion, the presented experiments demonstrate rigid zero bias peaks that are stable over an extended range in Zeeman energy and gate voltage in devices that show clear ballistic transport behavior. These observations exclude explanations for our zero bias peaks that are based on quantum confinement[14], Kondo effects[15], or disorder[11–13]. We know of no theoretical framework other than those based on Majorana fermions that is consistent with our observations.

Methods

Nanowire growth and device fabrication. InSb nanowires have been grown by Au-catalyzed Vapor-Liquid-Solid mechanism in a Metal Organic Vapor Phase Epitaxy reactor. The InSb nanowire crystal direction is [111] zinc blende, free of stacking faults and dislocations[27]. Nanowires are deposited one-by-one using a micro-manipulator on a substrate covered with 285 nm thick SiO_2 serving as a gate dielectric for back gated devices. For local gated devices, extra set of bottom gates are patterned on the substrate followed by transfer of h-BN ($\sim$ 30 nm thick) onto which nanowires are deposited. Contact deposition process starts with resist development followed by Oxygen plasma cleaning. Then, the chip is immersed in a Sulfur-rich ammonium sulfide solution diluted by water (with a ratio of 1:200) at 60 °C for half an hour[28]. At all stages care is taken to expose the solution to air as little as possible. For normal metal contacts, the chip is placed into an evaporator. A 30 second Helium ion milling is performed in-situ before evaporation of Cr/Au (10 nm/125 nm) at a base pressure $< 10^{-7}$ mbar. For superconducting contacts, the chip is mounted in a sputtering system. After 5 seconds of in-situ Ar plasma etching at a power of 25 Watts and an Ar pressure of 10 mTorr, 5 nm NbTi is sputtered followed by 85 nm NbTiN.

Measurement setup and data analysis. All the data in this Letter is measured in a dilution refrigerator with a base temperature around 50 mK using several stages of filtering. The determination of the Andreev enhancement factor depends sensitively on the contact resistance subtracted from the measured data. In all our analysis we only subtract a fixed-value series resistance of 0.5 kOhm solely to account for the contact resistance of the normal metal lead. This value is smaller than the lowest contact resistance we have ever obtained for InSb nanowire devices[22,23], which makes the values for the interface transparency a lower bound.

Structure characterization. The cross-section and lamella for TEM investigations were prepared by focused ion beam (FIB). FIB milling was carried out with a FEI Nova Nanolab 600i Dualbeam with a Ga ion beam following the standard procedure[29]. We used electron induced Co and Pt deposition for protecting the region of interest and a final milling step at 5 kV to limit damage to the lamella. High-resolution TEM (HRTEM) and scanning TEM (STEM) analyses were conducted using a JEM ARM200F aberration-corrected TEM operated

at 200 kV. For the chemical analysis, energy dispersive X-ray (EDX) measurements were carried out using the same microscope equipped with a 100 mm^2 EDX silicon drift detector (SSD).

Characterization of NbTiN. Our NbTiN films are deposited using an ultrahigh vacuum AJA International ATC 1800 sputtering system (base pressure $\sim 10^{-9}$ Torr). We use a $Nb_{0.7}Ti_{0.3}$ wt. % target with a diameter of 3 inches. Reactive sputtering resulting in nitridized NbTiN films was performed in an Ar/N process gas with 9 at. % nitrogen content at a pressure of 2.5 mTorr using a DC magnetron sputter source at a power of 250 Watts. An independent characterization of the NbTiN films gave a critical temperature of 13.3 K for 90 nm thick films with a resistivity of 126 μOhm·cm and a compressive stress on Si substrate.

[1] Read, N. & Green, D. Paired states of fermions in two dimensions with breaking of parity and time-reversal symmetries and the fractional quantum Hall effect. *Phys. Rev. B* **61**, 10267 (2000)

[2] Kitaev, A. Y. Unpaired Majorana fermions in quantum wires. *Phys. Usp.* **44**, 131 (2001)

[3] Fu, L. & Kane, C. L. Superconducting proximity effect and Majorana fermions at the surface of a topological insulator. *Phys. Rev. Lett.* **100**, 096407 (2008)

[4] Lutchyn, R. M., Sau, J. D. & Das Sarma, S. Majorana fermions and a topological phase transition in semiconductor-superconductor heterostructures. *Phys. Rev. Lett.* **105**, 077001 (2010)

[5] Oreg, Y., Refael, G. & von Oppen, F. Helical liquids and Majorana bound states in quantum wires. *Phys. Rev. Lett.* **105**, 177002 (2010)

[6] Mourik, V. *et al.* Signatures of Majorana fermions in hybrid superconductor-semiconductor nanowire devices. *Science* **336**, 1003 (2012)

[7] Das, A. *et al.* Zero-bias peaks and splitting in an Al-InAs nanowire topological superconductor as a signature of Majorana fermions. *Nature Phys.* **8**, 887 (2012)

[8] Deng, M. T. *et al.* Anomalous zero-bias conductance peak in a Nb–InSb nanowire–Nb hybrid device. *Nano Lett.* **12**, 6414 (2012)

[9] Churchill, H. O. H. *et al.* Superconductor-nanowire devices from tunneling to the multichannel regime: Zero-bias oscillations and magnetoconductance crossover. *Phys. Rev. B* **87**, 241401 (2013)

[10] Finck, A. D. K., Van Harlingen, D. J., Mohseni, P. K., Jung, K. & Li, X. Anomalous modulation of a zero-bias peak in a hybrid nanowire-superconductor device. *Phys. Rev. Lett.* **110**, 126406 (2013)

[11] Liu, J., Potter, A. C., Law, K. T. & Lee, P. A. Zero-bias peaks in the tunneling conductance of spin-orbit-coupled superconducting wires with and without Majorana end-states. *Phys. Rev. Lett.* **109**, 267002 (2012)

[12] Pikulin, D. I., Dahlhaus, J. P., Wimmer, M., Schomerus, H. & Beenakker, C. W. J. A zero-voltage conductance peak from weak antilocalization in a Majorana nanowire. *New J. Phys.* **14**, 125011 (2012)

[13] Bagrets, D. & Altland, A. Class D spectral peak in Majorana quantum wires. *Phys. Rev. Lett.* **109**, 227005 (2012)

[14] Lee, E. J. H. *et al.* Spin-resolved Andreev levels and parity crossings in hybrid superconductor-semiconductor nanostructures. *Nature Nanotech.* **9**, 79 (2014)

[15] Lee, E. J. H. *et al.* Zero-Bias anomaly in a nanowire quantum dot coupled to superconductors. *Phys. Rev. Lett.* **109**, 186802 (2012)

[16] Takei, S., Fregoso, B. M., Hui, H.-Y., Lobos, A. M. & Das Sarma, S. Soft superconducting gap in semiconductor Majorana nanowires. *Phys. Rev. Lett.* **110**, 186803 (2013)

[17] Cheng, M., Lutchyn, R. M. & Das Sarma, S. Topological protection of Majorana qubits. *Phys. Rev. B* **85**, 165124 (2012)

[18] Rainis, D. & Loss, D. Majorana qubit decoherence by quasiparticle poisoning. *Phys. Rev. B* **85**, 174533 (2012)

[19] Chang, W. *et al.* Hard gap in epitaxial semiconductor–superconductor nanowires. *Nature Nanotech.* **10**, 232 (2015)

[20] Albrecht, S. M. *et al.* Exponential protection of zero modes in Majorana islands. *Nature* **531**, 206 (2016)

[21] Gül, Ö. *et al.* Towards high mobility InSb nanowire devices. *Nanotechnology* **26**, 215202 (2015)

[22] van Weperen, I., Plissard, S. R., Bakkers, E. P. A. M., Frolov, S. M. & Kouwenhoven, L. P. Quantized conductance in an InSb nanowire. *Nano Lett.* **13**, 387 (2013)

[23] Kammhuber, J. *et al.* (submitted)

[24] Beenakker, C. W. J. Quantum transport in semiconductor-superconductor microjunctions. *Phys. Rev. B* **46**, 12841 (1992)

[25] Zuo, K. & Mourik, V. *Signatures of Majorana fermions in hybrid superconductor-semiconductor nanowire devices.* PhD dissertation, Delft University of Technology (2016)

[26] Micolich, A. P. What lurks below the last plateau: experimental studies of the $0.7 \times 2e^2/h$ conductance anomaly in one-dimensional systems. *J. Phys. Condens. Matter* **23**, 443201 (2011)

[27] Car, D., Wang, J., Verheijen, M. A., Bakkers, E. P. A. M. & Plissard, S. R. Rationally designed single-crystalline nanowire networks. *Adv. Mater.* **26**, 4875 (2014)

[28] Suyatin, D. B., Thelander, C., Björk, M. T., Maximov, I. & Samuelson, L. Sulfur passivation for ohmic contact formation to InAs nanowires. *Nanotechnology* **18**, 105307 (2007)

[29] Giannuzzi, L. A., Drown, J. L., Brown, S. R., Irwin, R. B. & Stevie, F. A. Applications of the FIB lift-out technique for TEM specimen preparation. *Microsc. Res. Tech.* **41**, 285 (1998)

Acknowledgments

We thank A. Akhmerov, M. de Moor, J. Kammhuber, A. Geresdi, M. Cassidy, A. Storm, S. Koelling, and O. Benningshof for discussions and assistance. This work has been supported by the Netherlands Organisation for Scientific Research (NWO), Foundation for Fundamental Research on Matter (FOM), European Research Council (ERC) and Microsoft Corporation Station Q.

Author contributions

H.Z. and Ö.G. fabricated the devices, performed the measurements, and analyzed the data. S.C.-B. performed the TEM analysis. K.Z., V.M., F.d.V., J.v.V., D.v.W., M.Q.-P., and S.G. contributed to the experiments. M.N. and M.W. performed the numerical simulations. D.C., S.P., and E.B. grew the InSb nanowires. K.W. and T.T. synthesized the h-BN crystals. L.P.K. supervised the project. All authors contributed to the writing of the manuscript.

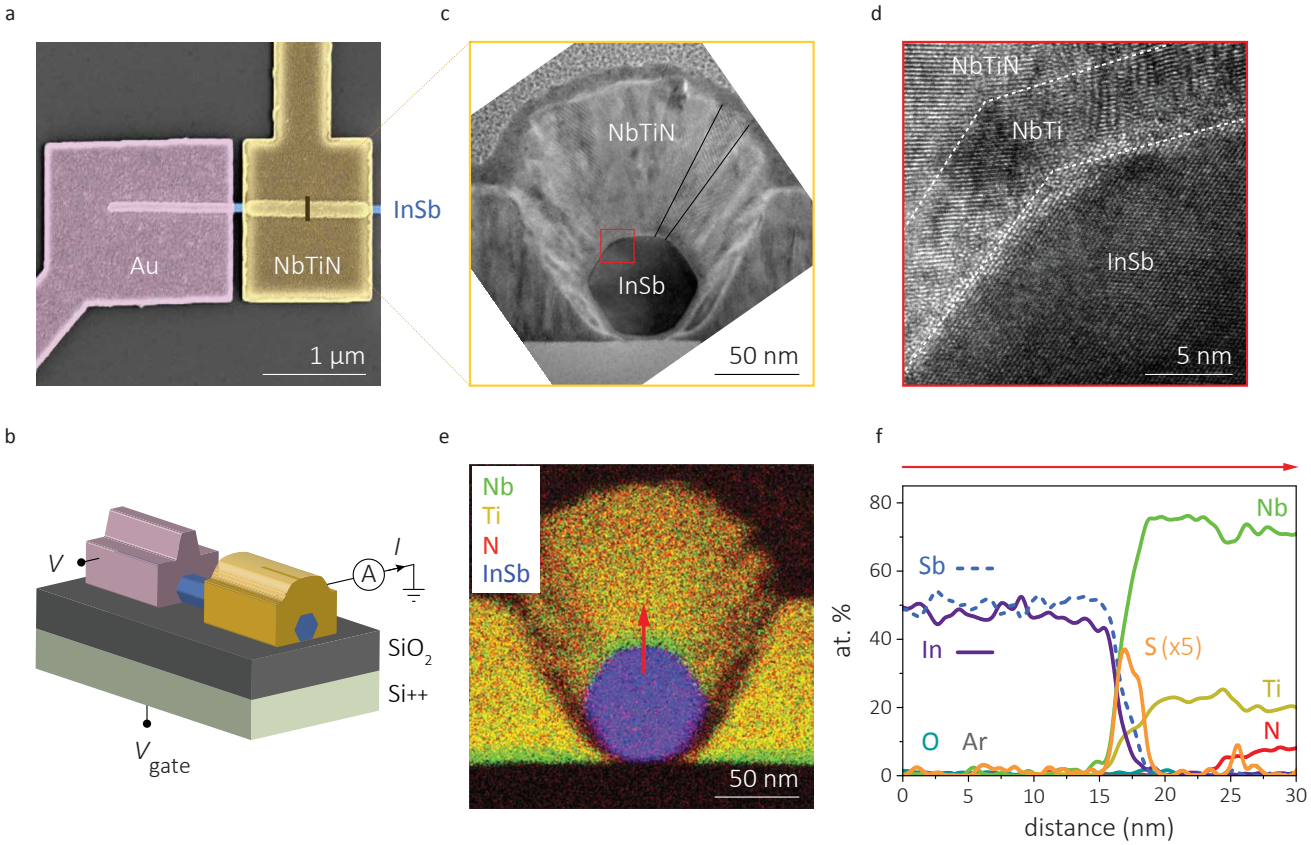

Figure 1: **TEM analysis of a Majorana device. a,** Top-view, false-colour electron micrograph of device A. Normal metal contact is Cr/Au (10 nm/125 nm) and superconducting contact is NbTi/NbTiN (5 nm/85 nm). Contact spacing is ~ 100 nm. **b,** Device schematic and measurement setup. **c,** Low-magnification HR TEM cross-sectional image from the device (see Methods). The cut was performed perpendicular to the nanowire axis, indicated by the dark bar in **a**. InSb NW exhibits a hexagonal cross-section surrounded by {220} planes. The NbTiN on the pre-layer NbTi crystallizes as cone-like elongated grains, indicated by the thin black lines. Corresponding fast Fourier transform confirms the polycrystalline character of the NbTiN region (Supplementary Figure 1b). **d,** High-resolution TEM image near the interface (red square in **c**) shows our cleaning and contact deposition procedure leaves the InSb crystal structure intact. **e,** EDX compositional map of the device cross-section. **f,** EDX line scan taken across the interface as indicated by the red arrow in **e**. The Sulfur content is multiplied by 5 for clarity. The system is Oxygen and Argon free (contact deposition is performed in an Ar plasma environment).

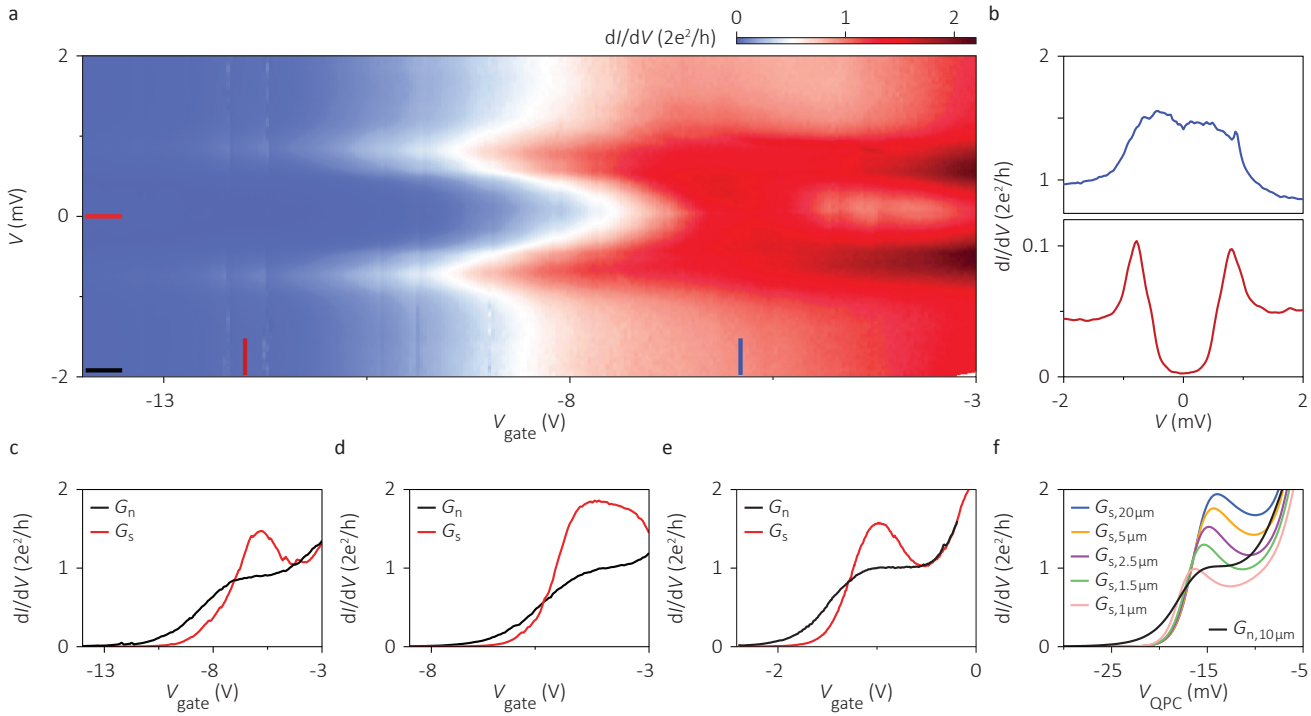

Figure 2: **Ballistic transport in Majorana devices at zero magnetic field. a,** Differential conductance, $\mathrm{d}I/\mathrm{d}V$, as a function of bias voltage, V, and gate voltage, V_{gate} for device B. **b,** Vertical line cuts from **a** on the conductance plateau (blue trace, gate voltage $= -5.9\,\mathrm{V}$) and in tunnelling regime (red trace, gate voltage $= -12\,\mathrm{V}$). **c,** Horizontal line cuts from **a** showing above-gap (G_{n}, black, $|V| = 2\,\mathrm{mV}$) and subgap (G_{s}, red, $V = 0\,\mathrm{mV}$) conductance. **d,** Above-gap (black) and subgap (red) conductance for device C, where G_{s} enhancement reaches $1.9 \times 2e^2/h$. **e,** Above-gap (black) and subgap (red) conductance for device E where above-gap conductance shows a very flat plateau. **f,** Numerical simulation for devices with different mean free paths (see Supplementary Figure 5). Black trace is for G_{n} corresponding to a mean free path $10\,\mu$m, the rest are for G_{s} corresponding to a mean free path ranging from $1\,\mu$m (pink) to $20\,\mu$m (blue).

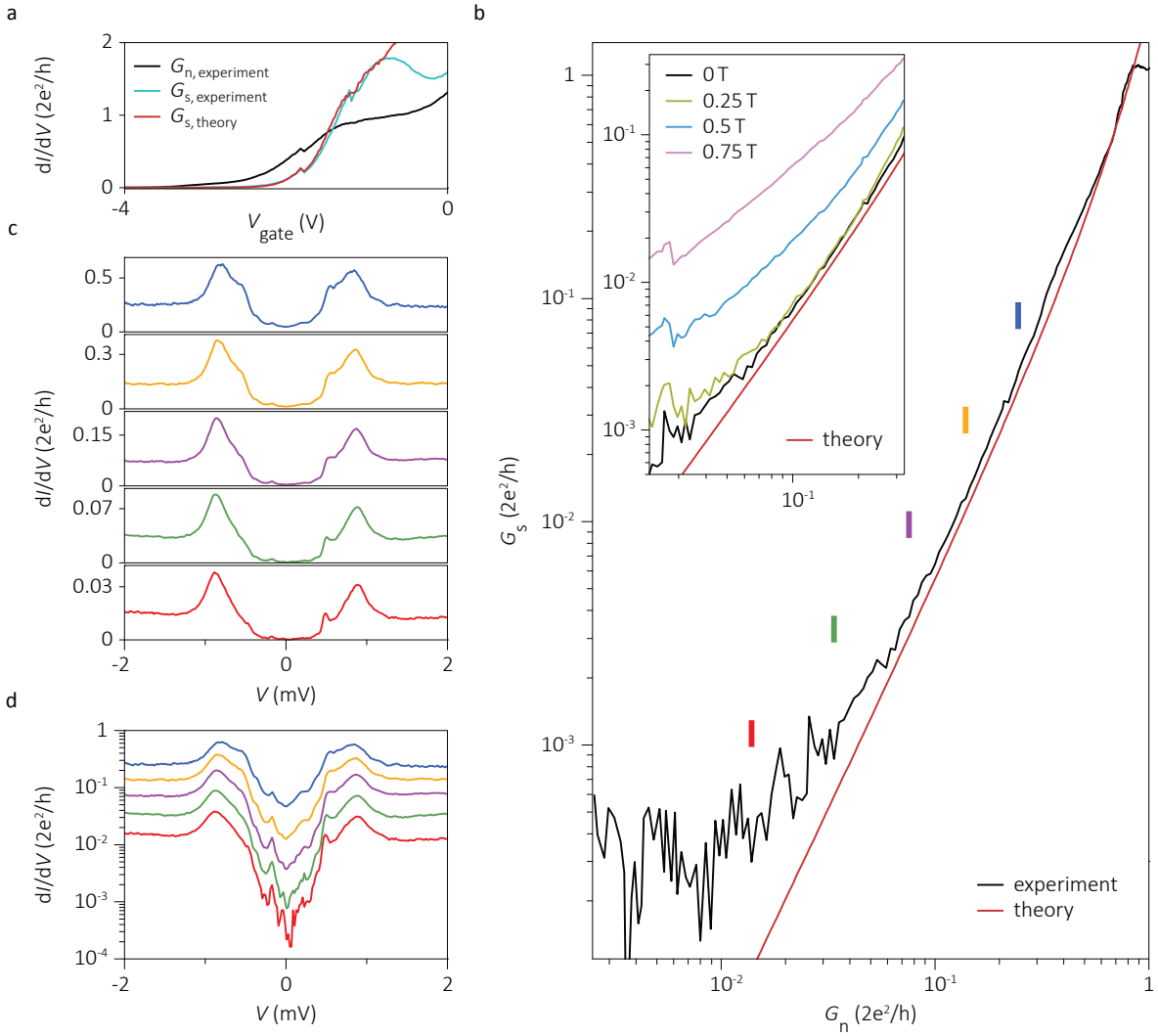

Figure 3: **Hard gap and Andreev transport. a,** Above-gap (black) and subgap (blue) conductance for device D. Red curve is a theory prediction based on single channel Andreev reflection, agreeing perfectly with experimental data without any fitting parameter. **b,** Subgap conductance G_s as a function of above-gap conductance G_n for device A. Red curve is the theory prediction assuming only Andreev processes. Inset shows G_s versus G_n taken at different magnetic fields. **c, d,** Five typical gap traces corresponding to the five colour bars indicated in **b** plotted on a linear and logarithmic scale. The subgap conductance is suppressed by a factor up to 50 for the lowest conductance (red trace).

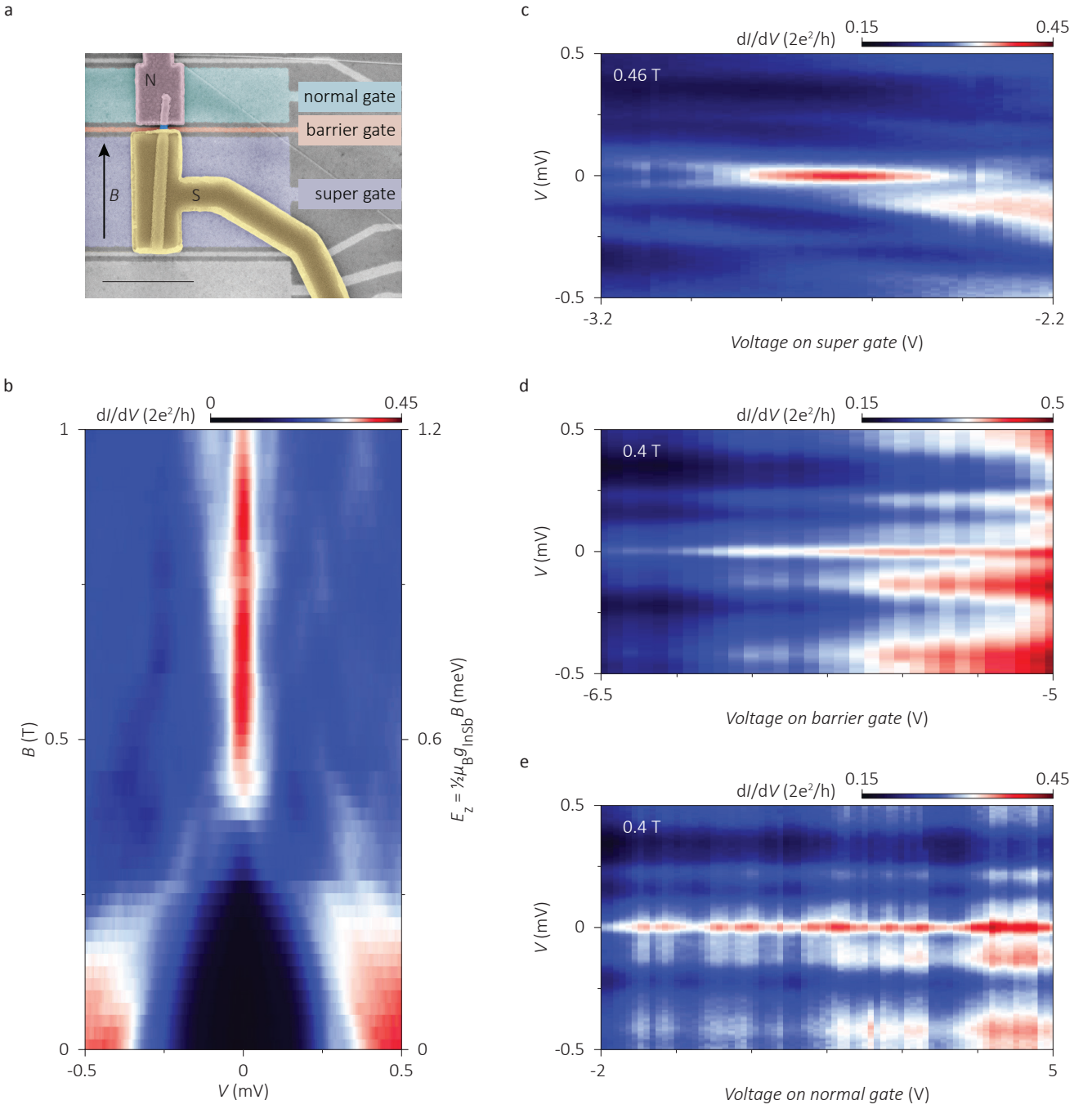

Figure 4: **Zero-bias-peak stability in gate voltage and magnetic field. a,** False-colour electron micrograph of a typical multi-gate Majorana device (scale bar 1 μm). The three bottom gates (normal gate, barrier gate, and super gate) are covered by a thin boron-nitride flake acting as a dielectric layer. Magnetic field B is parallel to the nanowire within 10 degrees and is expected to be roughly perpendicular to the direction of the spin-orbit field. **b,** $\mathrm{d}I/\mathrm{d}V$ as a function of V and B. Gate voltages are fixed at $-2.8\,\mathrm{V}$, $-5.5\,\mathrm{V}$, and $1\,\mathrm{V}$ for super, barrier, and normal gate, respectively. The right axis scales with Zeeman energy assuming $g_{\mathrm{InSb}} = 40$. **c,** $\mathrm{d}I/\mathrm{d}V$ as a function of super gate voltage for $B = 0.46\,\mathrm{T}$, barrier gate and normal gate voltages are $-5.5\,\mathrm{V}$ and $1\,\mathrm{V}$, respectively. **d,** $\mathrm{d}I/\mathrm{d}V$ as a function of barrier gate voltage for $B = 0.4\,\mathrm{T}$, normal and super gate voltages are $2.5\,\mathrm{V}$ and $-2.85\,\mathrm{V}$, respectively. **e,** $\mathrm{d}I/\mathrm{d}V$ as a function of normal gate voltage for $B = 0.4\,\mathrm{T}$, barrier and super gate voltages are $-5.5\,\mathrm{V}$ and $-2.85\,\mathrm{V}$, respectively. Data in this figure is taken on device F. Corresponding line cuts can be found in Supplementary Figure 6.

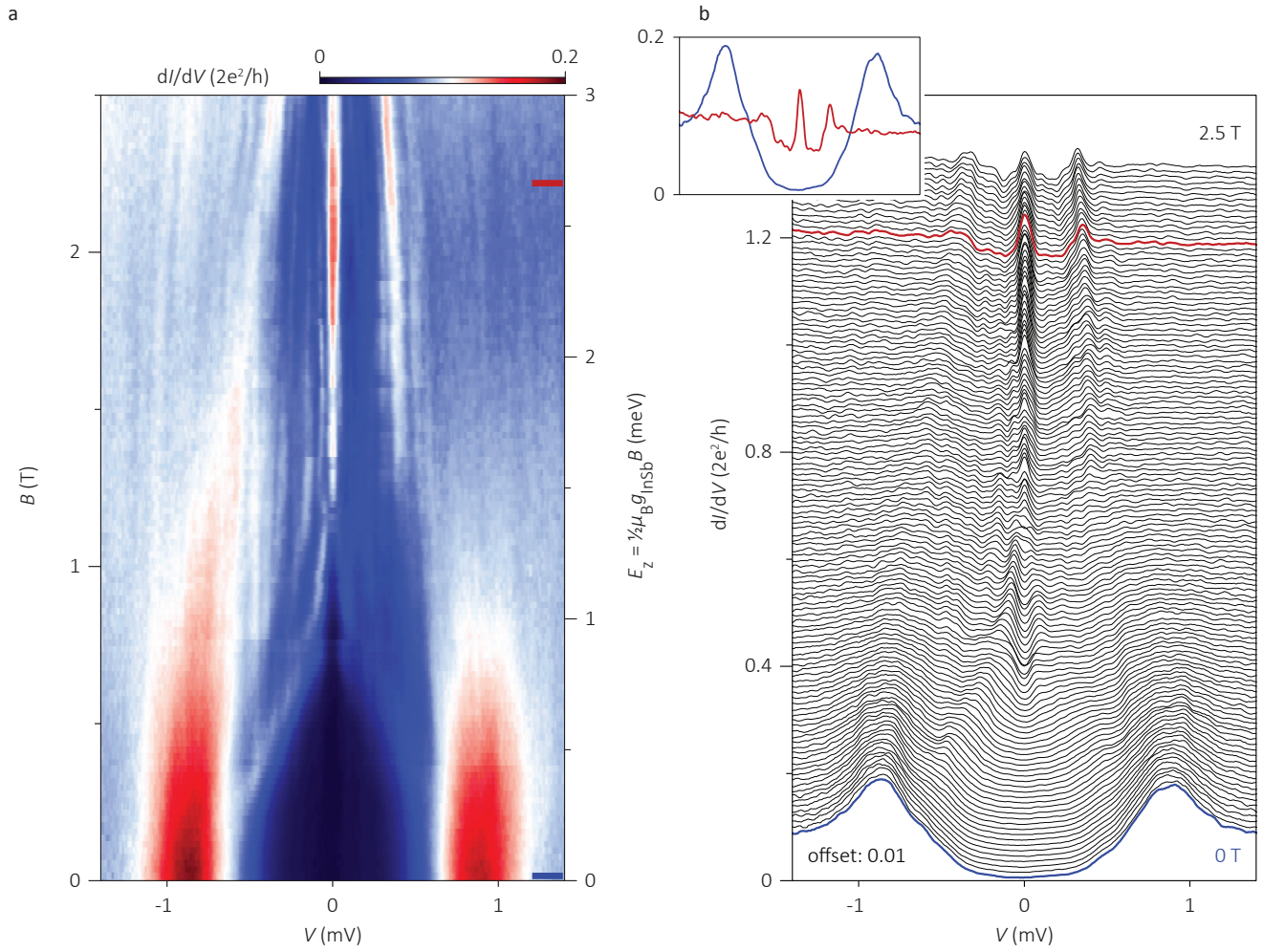

Figure 5: **Zero-bias-peak behaviour up to 2.5 T. a,** ZBP measured on device G. The induced gap size $\Delta^* = 0.9\,\mathrm{meV}$. An un-split ZBP is visible between 1.2 and 2.5 Tesla. **b,** Line cuts from the data in **a** with vertical offsets $0.01 \times 2e^2/h$. Inset compares the traces at zero magnetic field (blue) and 2.22 Tesla (red) without offset. The gate voltages on super, normal, and barrier gate are $-7\,\mathrm{V}$, $5\,\mathrm{V}$, and $-1.17\,\mathrm{V}$, respectively. Magnetic field is along the nanowire.

Supplementary Information: Ballistic Majorana nanowire devices

Hao Zhang,[1,2,*] Önder Gül,[1,2,*] Sonia Conesa-Boj,[1,2,3] Kun Zuo,[1,2] Vincent Mourik,[1,2] Folkert K. de Vries,[1,2] Jasper van Veen,[1,2] David J. van Woerkom,[1,2] Michał P. Nowak,[1,2] Michael Wimmer,[1,2] Diana Car,[3] Sébastien Plissard,[2,3] Erik P. A. M. Bakkers,[1,2,3] Marina Quintero-Pérez,[1,4] Srijit Goswami,[1,2] Kenji Watanabe,[5] Takashi Taniguchi,[5] Leo P. Kouwenhoven[1,2,†]

[1] *QuTech, Delft University of Technology, 2600 GA Delft, The Netherlands*
[2] *Kavli Institute of Nanoscience, Delft University of Technology, 2600 GA Delft, The Netherlands*
[3] *Department of Applied Physics, Eindhoven University of Technology, 5600 MB Eindhoven, The Netherlands*
[4] *Netherlands Organisation for Applied Scientific Research (TNO), 2600 AD Delft, The Netherlands*
[5] *Advanced Materials Laboratory, National Institute for Materials Science, 1-1 Namiki, Tsukuba, 305-0044, Japan*

[*]These authors contributed equally to this work. [†]Electronic address: L.P.Kouwenhoven@tudelft.nl

List of supplementary figures

Supplementary Figure 1 | Structure characterization and HAADF analysis of the InSb-NbTi-NbTiN interface.

Supplementary Figure 2 | Inclusion of Sulfur creates surface accumulation by band bending.

Supplementary Figure 3 | Electron micrograph of all presented devices.

Supplementary Figure 4 | Ballistic transport for all devices with global back gate.

Supplementary Figure 5 | Theoretical simulation of our devices.

Supplementary Figure 6 | Line cuts from Figure 4 (main text).

Supplementary Figure 7 | Zero bias peak is robust over a large conductance range.

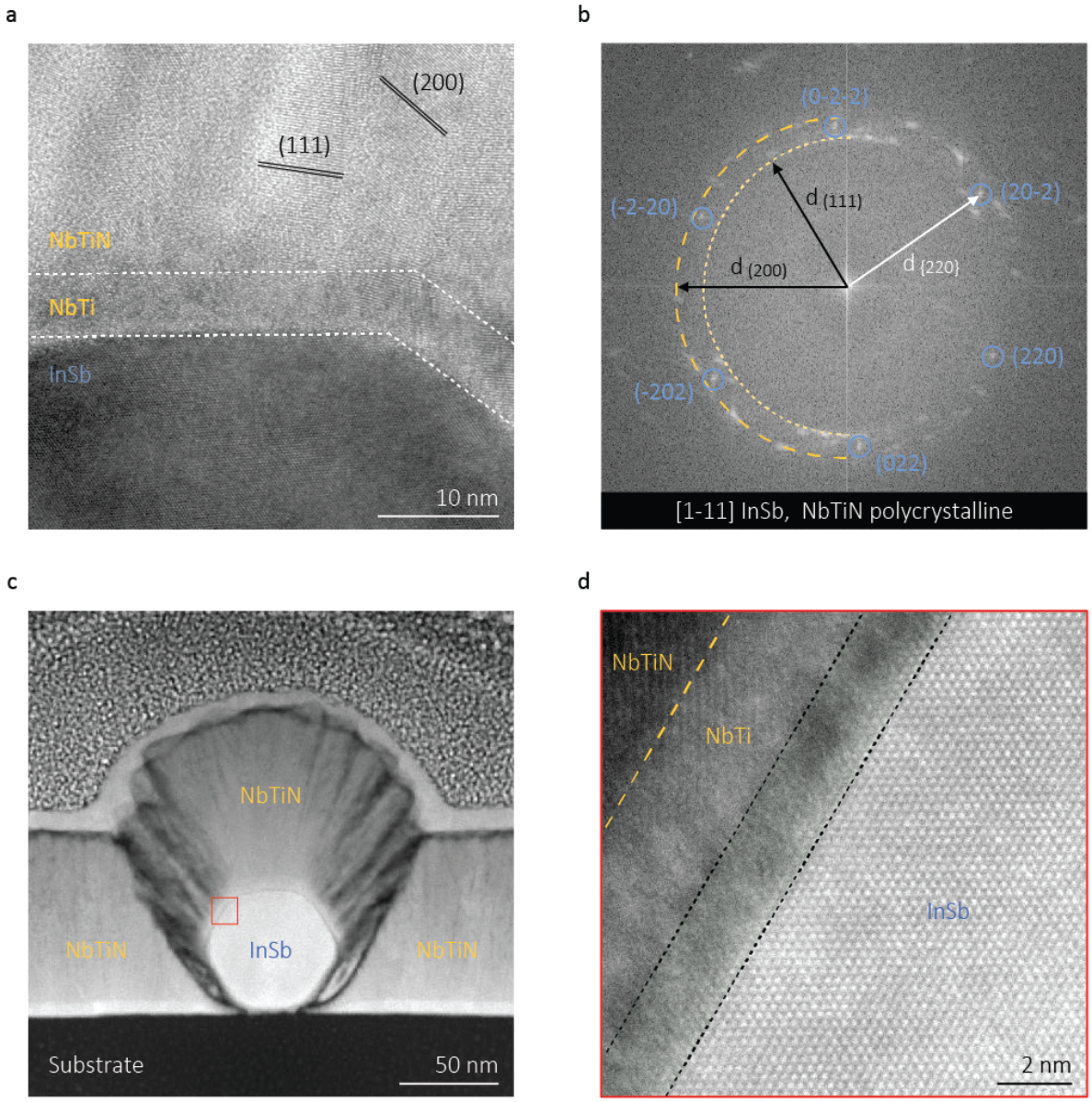

Supplementary Figure 1 | **Structure characterization and HAADF analysis of the InSb-NbTi-NbTiN interface. a,** High-resolution TEM (HR-TEM) cross-sectional image obtained by aligning the InSb nanowire along the zone axis in the [111] orientation. **b,** Fast Fourier transform (FFT) corresponding to **a** revealing the presence of both InSb and NbTiN. The NbTiN contribution leads to the formation of several Bragg spots on concentric rings, which provides evidence of the existence of several grains with different orientations in the original image. Each ring with different radius corresponds to a particular value of the interplanar spacing, i.e., it is the result of the reflections associated to a specific family of planes. Two different d-spacings have been identified and measured: $d_{(111)} = 0.249\,\text{nm}$ and $d_{(200)} = 0.213\,\text{nm}$. They are indicated with yellow dashed lines in **b**. From these values, it is possible to determine the NbTiN lattice parameter which we obtain to be 0.430 nm. On the other hand, the six {220} reflections, indicated by a blue circle in the FFT, arise from the InSb region. From the calculated interplanar value of $d_{\{220\}} = 0.230\,\text{nm}$ we can estimate the InSb lattice

parameter to be around 0.649 nm. The obtained lattice parameters for both NbTiN and InSb are in good agreement with the respective values reported in the literature. **c,** High-angle annular dark field (HAADF) scanning transmission electron microscopy (STEM) image of the device cross-section. **d,** Atomic resolution HAADF-STEM image of the interface for the region marked by the red square in **c**. The highlighted area in green indicates the 2 nm deep NbTi segregation into the InSb core. This effect is in good agreement with the EDX line scan, see Figure 1f (main text), which shows the NbTi region to be segregated 2 nm deep into the InSb core on the {220} facets. Interestingly, this value of the fraction of Nb in InSb could lead to the formation of a *half-breed* ternary superconductor at the interface, which would thus substantially improve its quality by increasing the effective contact area.

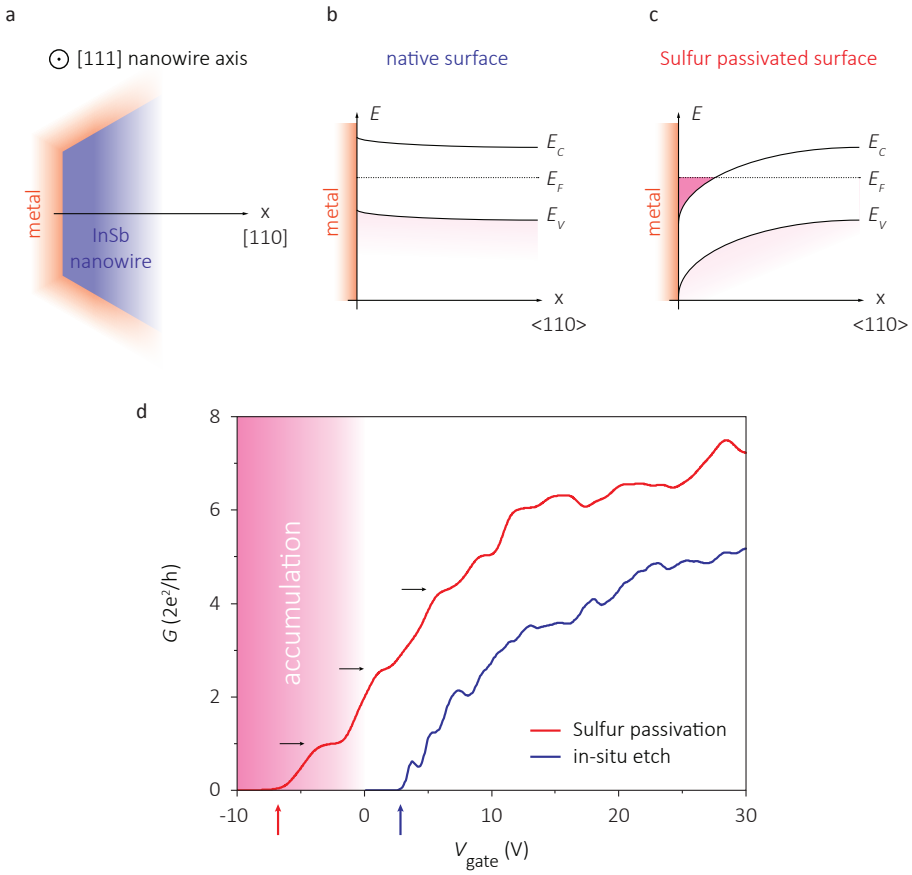

Supplementary Figure 2 | **Inclusion of Sulfur creates surface accumulation by band bending. a,** A schematic of the device cross-section showing both the nanowire and the contact metal. Nanowire axis is along [111] and the hexagonal facets have <110> orientation. **b,** Band diagram for an InSb surface with <110> orientation. Fermi level at the surface lies closer to valence band[1]. **c,** Band diagram for an InSb surface with <110> orientation passivated with Sulfur-based solution. Inclusion of Sulfur at the surface counteracts the depletion and pins the Fermi level in the conduction band. This creates an electron-rich nanowire surface. **d,** Gate voltage response of nanowire devices with different contact preparation. A finite conductance for negative gate voltages indicates electron accumulation, highlighted in pink. Blue curve is taken from a device with contacts prepared using in-situ Ar plasma etch, red curve from a device with contacts prepared using Sulfur passivation. Both devices have identical geometries with a channel length of 150 nm. Devices with Sulfur passivated contact areas exhibit a negative threshold voltage (red arrow), in contrast to the devices with in-situ plasma etched contact areas (blue arrow). This typical characteristic measured on hundreds of nanowire devices indicates the doping effect of Sulfur inclusion at the InSb nanowire surface. Black arrows indicate the 1st, the 3rd, and the 5th quantized conductance plateau[2]. Upper plateaus appear at lower conductance values due to a finite contact resistance which is not subtracted from the conductance traces shown here. We also find that Sulfur passivated contacts show lower contact resistances than in-situ etched contacts, which can be seen from the difference in saturation conductance of both traces at high gate voltages.

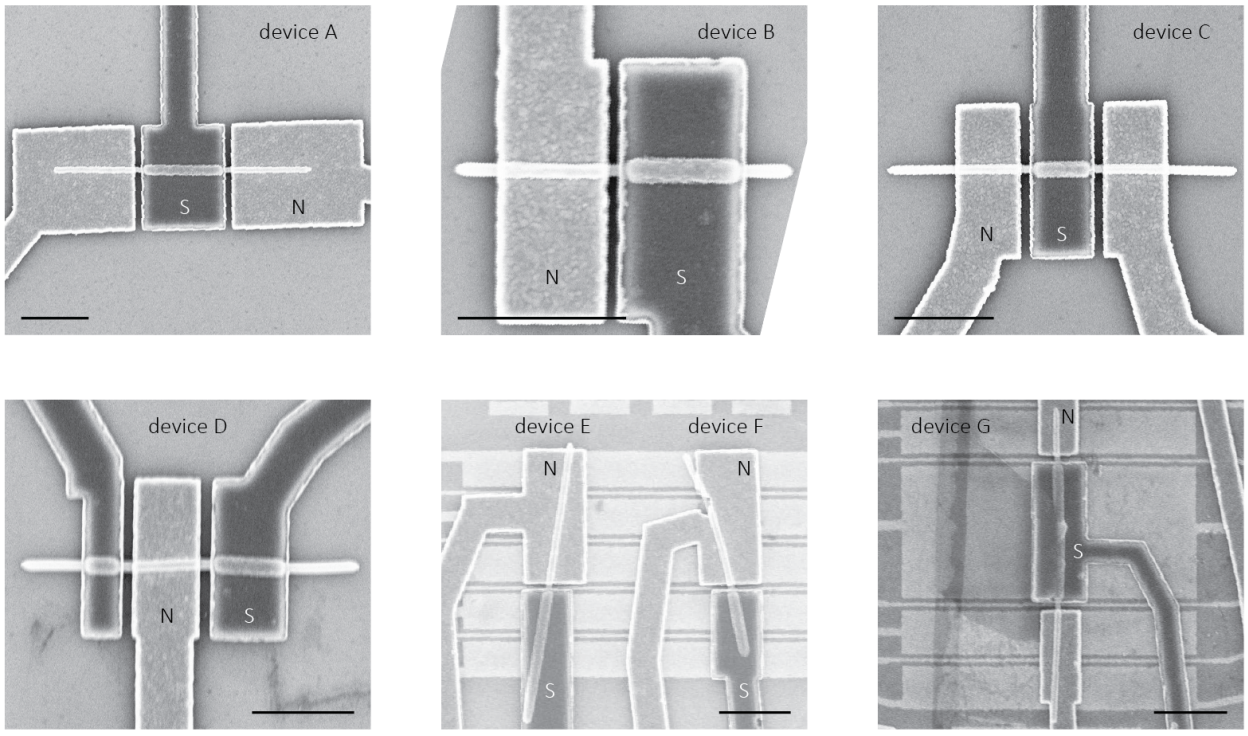

Supplementary Figure 3 | **Electron micrograph of all presented devices.** N indicates the normal metal lead, S the superconducting lead. For three terminal devices, unlabelled leads are kept floated throughout the measurements. Scale bars for all images indicate 1 μm. For devices E and F, the three gate electrodes underneath the superconducting contact are connected together in the external circuit. Data in Figure 2e (main text) is taken by sweeping the barrier gate underneath the uncovered wire section.

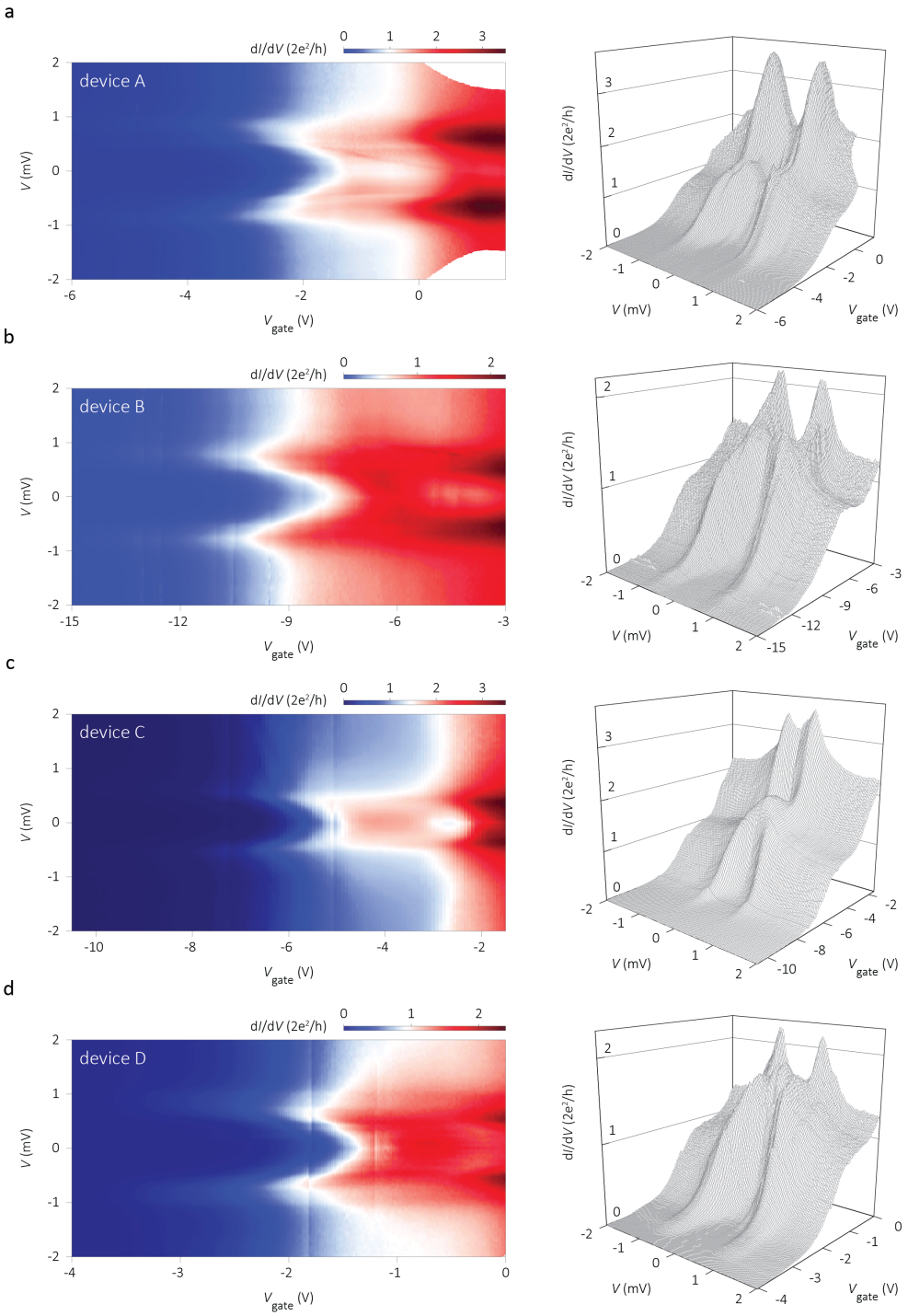

Supplementary Figure 4 | **Ballistic transport for all devices with global back gate. a-d,** Differential conductance of device A to D is shown in colour scale (left) and in height (right) as a function of bias and gate voltage at zero magnetic field. All devices show quantized conductance, Andreev enhancement and an induced superconducting gap of 0.9 mV (A), 0.8 mV (B), 0.6 mV (C) and 0.85 mV (D). Unintentional quantum dots are absent in all devices. Correspondence with the figures in main text: data in Figure 1 and Figures 3b-d taken on device A, Figures 2a-c on device B, Figure 2d on device C, Figure 3a on device D.

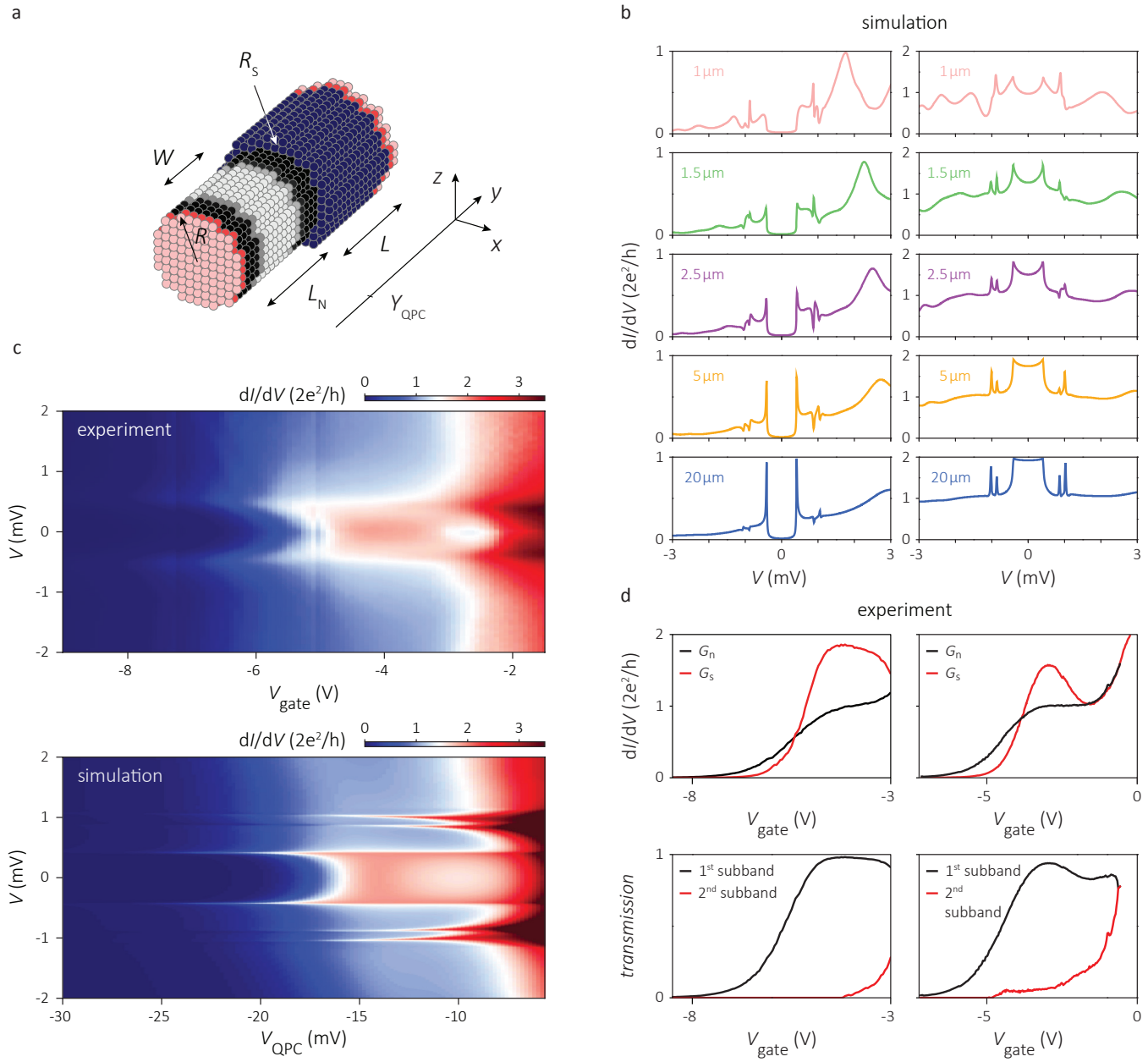

Supplementary Figure 5 | **Theoretical simulation of our devices. a,** Theoretical model: a cylindrical nanowire (black, gray, white) with length L_N+ L (100 nm + 800 nm), where the latter part is partially coated by a superconductor leaving the bottom surface uncovered. (Scheme shows $L = 100$ nm for clarity.) The wire radius R is 40 nm and the superconducting film has a thickness $R_s = 10$ nm. The wire is terminated from both sides with infinite leads (pink). Front lead is normal, back lead is normal/superconductor. Each little circle represents a three dimensional mesh site with a size of 7 nm. White circles depict a potential barrier with a width $W = 60$ nm in the uncovered wire section forming a quantum point contact (QPC). Gray circles represent the smoothness of the barrier which is set to 5 nm. **b,** Simulated differential conductance for different disorder strengths with mean free path l_e ranging from 1 μm (top) to 20 μm (bottom). The tunnelling conductance is shown on the left and the plateau regime on the right. For short l_e, the Andreev enhancement

is lower than that observed in our measurements and disorder-induced conductance fluctuations dominate the conductance for above-gap bias which we do not observe in our measurements. A good correspondence with the measurements is found for $l_e > 2.5\,\mu$m. We note that the details of the peak-dip structure in the Andreev conductance depend on several additional parameters of the system (e.g. barrier smoothness or disorder realization). In contrast, we find the conductance fluctuations above the gap to depend mainly on disorder strength, so that the combined analysis can be used as an estimate for the mean free path. The four symmetric peaks outside the gap around $V \sim \pm 1\,$mV indicate the induced superconducting gap for the higher two subbands (three subbands are occupied in total). Asymmetric conductance for different bias polarity is due to energy dependent transmission through the tunnel barrier (see also bottom panel of **c**), i.e., for positive bias V, effective QPC potential is lower. **c,** Comparison between the measurement (device C) and the simulation of a ballistic device with $l_e = 10\,\mu$m. Experiment agrees well with theory indicating a very low disorder strength for our devices. The induced superconducting gap edges for higher subbands, visible in the simulation, are not observed in the experiment. **d,** Mode-mixing induced dip in Andreev conductance. Upper panels show the measured data taken from the main text, the left from Figure 2d and the right from Figure 2e. Lower panels show the transmission T of the first two subbands extracted from the upper panels using $G_\mathrm{n} = 2e^2/h \sum T_i$ and $G_\mathrm{s} = 4e^2/h \sum T_i^2/(2-T_i)^2$. When the transmission of the second subband becomes finite, the conductance modes mix, decreasing the Andreev enhancement. This effect shows up as a dip in G_s when plotted as a function of gate voltage V_gate.

Details of the theoretical simulation. The system is described by the spin-diagonal Bogoliubov-de Gennes Hamiltonian

$$H = \left(\frac{\hbar^2 \mathbf{k}^2}{2m^*} - \mu + V(x,y,z) \right) \tau_z + \Delta(x,y,z)\tau_x \tag{1}$$

acting on the spinor $\Psi = (\psi_{e+}, \psi_{e-}, \psi_{h-}, -\psi_{h+})^T$. The Pauli matrices act on the electron-hole degree of freedom. Potential in the nanowire is described by $V(x,y,z) = \tilde{V}_{qpc}(y) + V_D(x,y,z)$, where $\tilde{V}_{qpc}(y)$ describes a quantum point contact given by

$$\tilde{V}_{qpc}(y) = -\frac{eV_\mathrm{QPC}}{2}\left[\tanh\frac{y - Y_{QPC} + W/2}{\lambda} - \tanh\frac{y - Y_{QPC} - W/2}{\lambda} \right].$$

Here Y_QPC is the centre position of the barrier (Supplementary Figure **??**a). Barrier width is $W = 60\,$nm, and the barrier height is controlled by V_QPC. The softness of the barrier is given by λ which we take 5 nm. $V_D(x,y,z)$ accounts for disorder, which is modelled as a spatially varying potential with random values from a uniform distribution within a range $[-U_0, U_0]$ where amplitude $U_0 = \sqrt{3\pi/l_e m^{*2} a^3}$ is set by mean free path l_e.

We approximate the superconductor covering the wire by a layer of non-zero Δ for $(x^2 + z^2) > R$ and $y > L_N$ and $z > -R$. The huge wave vector difference in the superconductor and semiconductor cannot be captured in a numerical simulation. Hence, to capture the short coherence length in the superconductor, we take a superconducting shell of thickness $R_S = 10\,$nm and $\Delta = 200\,$meV. We then tune the induced gap to be close to the experimental value ($\sim 0.5\,$meV) by reducing the hopping between the semiconductor and the superconductor by a factor of 0.8.

The transport properties of the system are calculated using Kwant package[3] with the Hamiltonian in eq. (1) discretized on a 3D mesh with spacing $a = 7\,\mathrm{nm}$ and infinite input (normal) and output (normal/superconducting) leads. For a given V_{QPC} and excitation energy ε we obtain the scattering matrix of the system from which we subsequently extract electron $r_e(\varepsilon)$ and hole $r_h(\varepsilon)$ reflection submatrices. Finally, we calculate thermally averaged conductance for injection energy $E = eV$ according to

$$G(E) = \int d\varepsilon \mathcal{G}(\varepsilon) \left(-\frac{\partial f(E,\varepsilon)}{\partial \varepsilon} \right),$$

where the Fermi function

$$f(E,\varepsilon) = \frac{1}{e^{(\varepsilon - E)/k_b T} + 1}$$

and $\mathcal{G}(\varepsilon) = N - \|r_e(\varepsilon)\|^2 + \|r_h(\varepsilon)\|^2$. We assume chemical potential to be $\mu = 30$ meV, which gives $N = 3$ spin-degenerate modes in the leads. The presented results are obtained for $T = 70\,\mathrm{mK}$ and InSb effective mass $m^* = 0.014 m_e$.

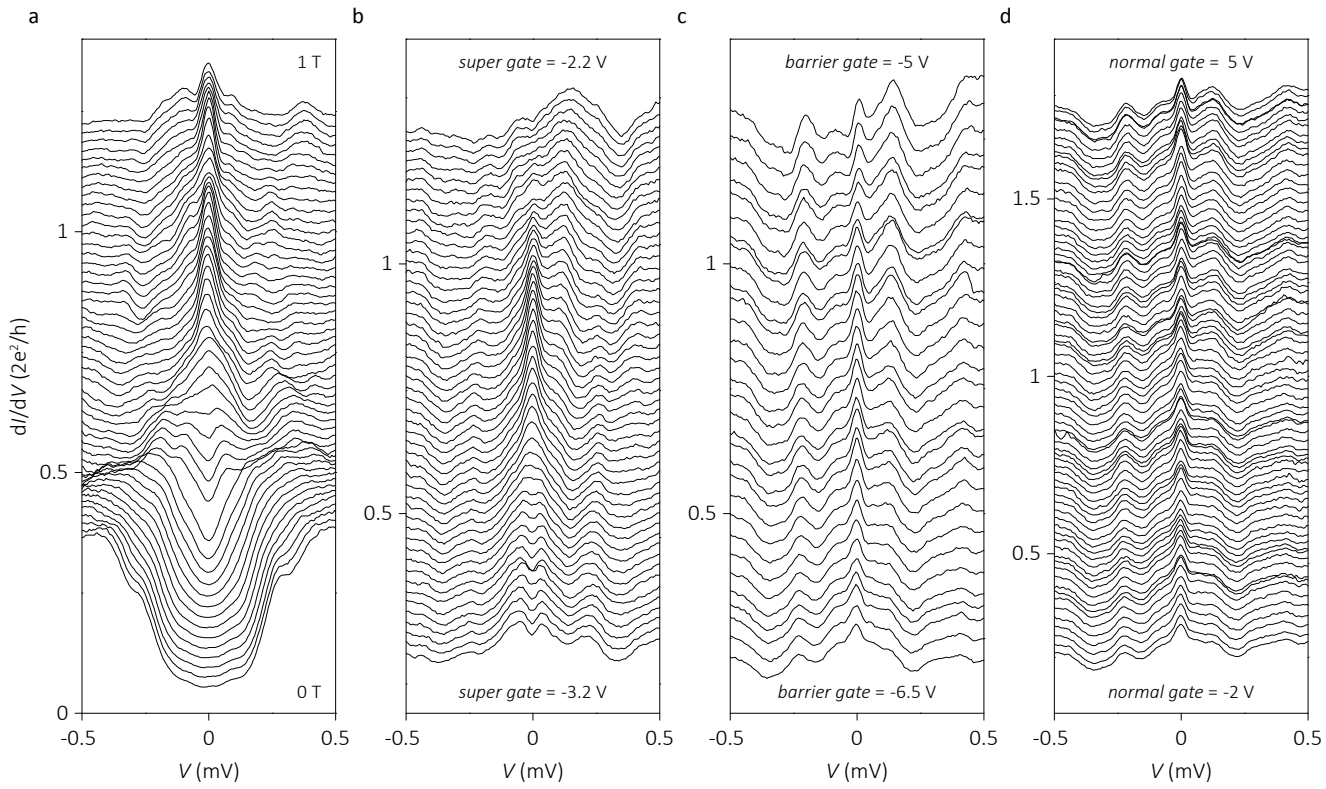

Supplementary Figure 6 | **Line cuts from Figure 4 (main text). a-d,** Line cuts which correspond to Figures 4b-e (main text), respectively. Vertical offset for **a-d** are: 0.02, 0.02, 0.03, and 0.02 (in units of $2e^2/h$). The typical zero bias peak height is around $0.1 \times 2e^2/h$ with a full width half maximum around $50\,\mu$V. This suggests that the zero bias peak is not only temperature broadened ($3.5k_BT \sim 15\,\mu$eV).

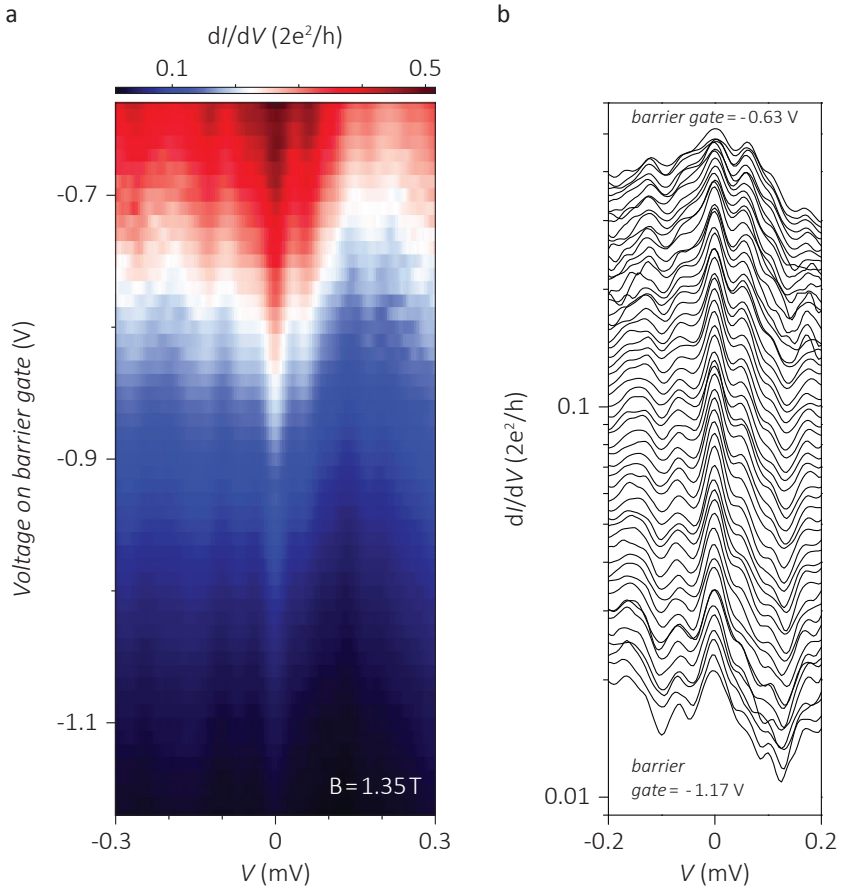

Supplementary Figure 7 | **Zero bias peak is robust over a large conductance range. a,** Differential conductance as a function of barrier gate voltage for the device presented in Figure 5 (main text). Magnetic field $B = 1.35\,\mathrm{Tesla}$, *super gate voltage* $= -6.4\,\mathrm{V}$, *normal gate voltage* $= 2.5\,\mathrm{V}$. **b,** Line cuts from **a** in logarithmic scale without an offset. Zero bias peak is robust over a conductance change by more than an order of magnitude.

[1] Gobeli, G. W. & Allen, F. G. Photoelectric properties of cleaved GaAs, GaSb, InAs, and InSb surfaces; comparison with Si and Ge. *Phys. Rev.* **137**, A245 (1965)

[2] Kammhuber, J. *et al.* (submitted)

[3] Groth, C. W., Wimmer, M., Akhmerov, A. R. & Weintal, X. Kwant: a software package for quantum transport. *New J. Phys.* **16**, 063065 (2014)